PERGAMON

Journal of Structural Geology 26 (2004) 71–85

JOURNAL OF STRUCTURAL GEOLOGY

www.elsevier.com/locate/jsg

Continuous restoration of deformed shapes through the construction of a reverse displacement gradient and its application to granite emplacement in central North China

Yehua Shan[a,b,*], Ge Lin[a], Zian Li[a], Hongbin Suen[a]

[a]*Changsha Institute of Geotectonics, Chinese Academy of Sciences, Changsha City 410013, P.R. China*
[b]*Department of Marine Geology, Ocean University of Qingdao, Qingdao City 266003, P.R. China*

Received 15 August 2002

Abstract

This paper presents a new technique to restore 2D/3D deformed shapes by minimization of the misfit between measured and theoretical reverse displacement gradients. Owing to its relatively direct and objective nature, the procedure ensures continuity of displacement across the boundaries between abutting elements. The procedure also minimizes the additional distortion of the elements that results from the compatibility of retro-deformation between abutting elements. We apply the technique to the Mesozoic Fangshan granodioritic pluton (FGP) in western Beijing, central North China. Based upon the measured strain of deformed enclaves, about 78% area of the present central zone can be restored by retro-deformation of the marginal and transitional zones. As a result of the emplacement of the central zone, deformation also occurred in both the outer zones and the wall rocks, predominantly by ductile flow. The associated deformation in the outer zones, with or without the involvement of the wall rocks, created space for the emplacement of the central zone. In addition, vertical expansion was effective in creating space for subsequent emplacement, producing approximately one third of the volume created by later expansion. Thus, ballooning is a viable mechanism for emplacement of the FGP.

Keywords: Deformed shape; Restoration; Reverse Displacement gradient; Optimization; Finite element

1. Introduction

Restoration of deformed shapes is fundamental to balancing cross-sections (Hossack, 1978; Woodward et al., 1986), and allows us to gain insight into the deformation field in which geological structures formed (Rouby et al., 2000). The lack of constraints, which are rather difficult to determine in the field, often gives rise to the possibility of a variety of solutions. Instead of more complex and sophisticated kinematic techniques, nearly all the techniques of retro-deformation presented till now are based upon finite strain analysis (Schwerdtner, 1977; Oertel and Ernst, 1978; Cobbold, 1979; Cobbold and Percevault, 1983; Woodward et al., 1986; Schultz-Ela, 1988; Schultz-Ela and Hudleston, 1991; Howard, 1993; Rouby et al., 2000; Lamb, 2001). They fall into two categories, discontinuous and continuous restoration.

Discontinuous restoration is referred to as the finite element approach (Oertel and Ernst, 1978; Cobbold, 1979; Cobbold and Percevault, 1983; Woodward et al., 1986; Schultz-Ela, 1988; Schultz-Ela and Hudleston, 1991; Rouby et al., 2000). The deformed region is discretized into a series of triangular or rectangle elements in plane problems, in which homogeneous deformation is assumed. There are two steps in the procedure, non-rotational unstraining of each element and subsequent fitting of abutting boundaries. The fitting step is the key to the approach. Continuous restoration, however, includes Howard's (1993) method of displacement analysis for restoring cross-sections, and Lamb's (2001) finite element approach for 2D deformed regions. Retro-deformation displacement functions are directly constructed by determining retro-deformational

* Corresponding author. Present address: Department of Marine Geology, Ocean University of Qingdao, Qingdao City 266003, P.R. China.
E-mail address: samcoun@public.qd.sd.cn (Y. Shan).

0191-8141/03/$ - see front matter © 2003 Elsevier Ltd. All rights reserved.
doi:10.1016/S0191-8141(03)00094-4

constants that relate undeformed states to present deformed states.

Although continuous in nature, Ismail-Zadeh et al.'s (2001) dynamic restoration is quite different from Howard's (1993) and Lamb's (2001) methods. It is a numerical approach that was designed for restoring profiles across diapiric salt structures through solving an inverse problem of the gravitational instability. The technique of Ismail-Zadeh et al. (2001) has a wide range of applicability, if the rocks can be approximated as continuously deformed. It is unable to incorporate discontinuous deformation such as faulting that is ubiquitous in the upper crust.

In general, both discontinuous restoration and continuous restoration have advantages and disadvantages. Discontinuous restoration is theoretically simple but difficult to write as a computer program. Since destraining and fitting are two separate steps, the restored shape of the deformed rocks is always dependent upon the fitting strategy as well as the scanning scheme for fitting unstrained blocks. Different fitting strategies on the minimization of gaps and/or overlaps between abutting elements lead to differences between different restored shapes. Further deformation of the unstrained elements is often necessary to fit their abutting boundaries. In the elements especially with a large variation of measured strain, gaps and/or overlaps between the neighboring unstrained elements often remain after restoration.

Continuous restoration is somewhat complicated in theory, which is perhaps the reason that a majority of existing techniques pertain to the discontinuous restoration category. However, it is fairly objective and easy to program. Both the compatibility and continuity of retro-deformation across the abutting boundaries are satisfied using this approach at the cost of homogenous deformation and of volume conservation in individual elements. Distinctive distortion required in restoring some elements is often far beyond the measured strain data (see the middle elements in Figs. 5 and 13 in Howard's (1993) paper for comparison). In Howard's (1993) method, the scheme of integration has some impact on the shapes of restored cross-sections.

We present a new technique for continuous restoration of 2D/3D deformed shapes by optimizing the misfit between theoretical and observed reverse displacement gradients. The method has broad applicability to the restoration of deformed objects. The finite element method is adopted to establish the theoretical reverse displacement gradient, whereas the observed displacement gradient is partly determined by the strain estimates. Variables such as rotational angles and reverse displacements are solved through iteration. Although somewhat similar to the method of Lamb (2001), our technique is distinctively based upon construction of the reverse displacement gradient by solving over-determined equations.

In order to show the validity of the technique, we apply it to the Mesozoic Fangshan granodioritic pluton in western Beijing, central North China. Based upon the measured strain of deformed enclaves, the result shows that 78% area of the present central zone can be accounted for by retro-deformation of the marginal and transitional zones. The emplacement of the central zone was forceful because the inflation involved not only the outer zones but the wall rock as well. This suggests that a ballooning mechanism would be valid for emplacement of the FGP.

2. New technique

2.1. Reverse displacement gradient

In the Cartesian system a material point P_0 with a coordinate (x_0, y_0, z_0) in the deformed state is transformed by retro-deformation into a new point P_1 with a coordinate (x_1, y_1, z_1) in the undeformed state. The reverse displacement (U, V, W), or the increment between P_0 and P_1 relative to a fixed reference frame in the deformed state, is expressed by:

$$U = x_1 - x_0 \qquad V = y_1 - y_0 \qquad W = z_1 - z_0 \tag{1}$$

In fact, a frequent aim of restoration techniques for deformed shapes is to find the solution of the displacement field or the reverse displacement field from measured strain data. The reverse displacement gradient is the partial differentiation of the reverse displacement, also called theoretical reverse displacement gradient T. It is defined as:

$$T = \left[t_{ij}\right]_{3\times3} = \begin{bmatrix} \frac{\partial U}{\partial x} & \frac{\partial U}{\partial y} & \frac{\partial U}{\partial z} \\ \frac{\partial V}{\partial x} & \frac{\partial V}{\partial y} & \frac{\partial V}{\partial z} \\ \frac{\partial W}{\partial x} & \frac{\partial W}{\partial y} & \frac{\partial W}{\partial z} \end{bmatrix} \tag{2}$$

Suppose a continuously deformed region of interest is discretized into a number of M k-node elements. The sizes of the elements are dependent upon the variation of measured strain. In the finite element analysis, the displacement of any point within an individual element can be interpolated from those at nodes (Zienkiewicz, 1977). Thus we have:

$$U = \sum_{i=1}^{k} N_i U_i \qquad V = \sum_{i=1}^{k} N_i V_i \qquad W = \sum_{i=1}^{k} N_i W_i \tag{3}$$

where U_i, V_i and W_i $(i = 1, 2,..., k)$ are displacements at the ith local node along the X-, Y- and Z-axes, and N_i $(i = 1, 2,..., k)$ is the shape function at the point P_0 (see Appendix B for the definition of the local function).

Hence the reverse displacement gradient may be written in another way:

$$T = \left[t_{ij}\right]_{3\times3} = \begin{bmatrix} \sum_{i=1}^{k} \frac{\partial N_i}{\partial x} U_i & \sum_{i=1}^{k} \frac{\partial N_i}{\partial y} U_i & \sum_{i=1}^{k} \frac{\partial N_i}{\partial z} U_i \\ \sum_{i=1}^{k} \frac{\partial N_i}{\partial x} V_i & \sum_{i=1}^{k} \frac{\partial N_i}{\partial y} V_i & \sum_{i=1}^{k} \frac{\partial N_i}{\partial z} V_i \\ \sum_{i=1}^{k} \frac{\partial N_i}{\partial x} W_i & \sum_{i=1}^{k} \frac{\partial N_i}{\partial y} W_i & \sum_{i=1}^{k} \frac{\partial N_i}{\partial z} W_i \end{bmatrix} \quad (4)$$

Homogeneity of deformation in an individual element is assumed, as in many restoration techniques. In order to satisfy this assumption, we select a linear local function and choose the 4-node tetrahedron element in 3D cases ($k = 4$) or the 3-node triangular element in 2D cases ($k = 3$). For the latter element, the linear local function is defined in Appendix B.

Strain data recorded in deformed rocks are first used to estimate the theoretical reverse displacement gradient. It includes the axial ratio of strain, the orientation of the principal strains, and the volume loss or gain. Rotation angle, the only unresolved parameter, is kept as an unknown variable in the gradient, and will be solved for during the restoration. Constraints are introduced, in order to obtain these unknown variables through solving for the reverse displacement field. We will discuss these constraints in the next section. Since evidence for volume loss or gain in deformed rocks is rather difficult to obtain, it will be neglected here. Furthermore, for simplicity we consider 2D cases that are familiar to most geologists to show the feasibility of the technique developed in the paper.

However, there is no difficulty in the application of our technique to 3D cases where 3D strain estimates are available. Some 3D deformed rocks can be reduced to 2D cases if the strain of the deformed bodies possesses some common feature, such as a constant principal direction normal to the section of interest. These reduced cases, similar to plane problems in elasticity, are still 3D in nature because the volume conservation assumption still holds. In terms of the known variables (strain data–axial ratio of strain and orientation of the principal strains) and the unknown variables (rotational angle) in an element, the components of the calculated reverse displacement gradient C in 2D, or $[c_{ij}]_{2\times2}$, are given in Appendix C:

$$\begin{aligned} c_{11} &= (t_1\cos^2\theta + t_2\sin^2\theta)\cos\psi - (t_1 - t_2)\sin\theta\cos\theta\sin\psi - 1 \\ c_{12} &= (t_1\cos^2\theta + t_2\sin^2\theta)\sin\psi + (t_1 - t_2)\sin\theta\cos\theta\cos\psi \\ c_{21} &= (t_1 - t_2)\sin\theta\cos\theta\cos\psi - (t_1\sin^2\theta + t_2\cos^2\theta)\sin\psi \\ c_{22} &= (t_1 - t_2)\sin\theta\cos\theta\sin\psi + (t_1\sin^2\theta + t_2\cos^2\theta)\cos\psi - 1 \end{aligned} \quad (5)$$

where θ is the orientation of the greatest principal strain, t_1 and t_2 are the half lengths of the greatest and the least principal strains, and ψ is the rotational angle of the element.

2.2. Objective function

By combining formulae (4) and (5), we have four nonlinear equations that describe the reverse displacement field in a 3-node triangular element. They are:

$$t_{ij}(U, V) = c_{ij}(\psi), \quad i,j = 1,2 \quad (6)$$

There are seven unknown variables in the above equations, including the displacements (U_i, V_i) ($i = 1, 2, 3$) and rotational angle ψ. For an extreme case with one single element, at least three of them should be specified in order to obtain a definite solution.

Let L stand for the total number of nodes and M for the total number of elements discretizing the study region. There are $4M$ equations, the number of unknown variables in which is $2L + M$. The number of equations exceeds that of unknown variables when many elements are included. There is no specific solution of the overdetermined equations since the nodes and the elements are fully free in 2D space. If they have a solution of (U, V, ψ), then ($U + \Delta U$, $V + \Delta V$, $\psi + \Delta\psi$) is also their solution, where (ΔU, ΔV) is any kind of translation of the elements and $\Delta\psi$ is any rotation of the elements. Therefore, before solving these overdetermined equations, we need to add necessary constraints to them. The constraints are specific to at least three variables in the equations. Even so, the number of unknown variables is still less than or equal to that of equations. There are many ways to choose and assign the three variables, depending upon the characteristics of deformational structures of interest. A common way, used below, is to let the displacement at one node and the rotational angle of one element be zero. Although different specifications may result in differing reverse displacement fields, the reverse displacement gradient obtained is always the same.

Let us define the objective function F as the sum of the squares of the difference betweens the components of theoretical and measured reverse displacement gradients, given in formulae (4) and (5). Thus the problem of the nonlinear equations turns out to be an optimization problem. It is:

$$\min.F = \sum_{l=1}^{M} \sum_{i=1}^{2} \sum_{j=1}^{2} (c_{ijl}(U(l), V(l)) - t_{ijl}\psi(l))^2 \quad (7)$$

Although there are a variety of algorithms to solve the optimization problem (e.g. Chen, 1996), we will develop a new strategy on the solution. If rotational angles, ψ, are known, the optimum displacements (U^*, V^*) are obtained

by solving the following equations:

$$\frac{\partial F}{\partial U(l)}\Big|_{\psi} = 0 \qquad \frac{\partial F}{\partial V(l)}\Big|_{\psi} = 0 \qquad l = 1, 2, \ldots, M \tag{8}$$

Since the above equations are explicitly linear and closed, they can be solved by some direct algorithms, such as the Gauss elimination method.

On the other hand, if the displacement (U, V) is known, the optimum rotational angles ψ^* are obtained by solving the following equation:

$$\frac{\partial F}{\partial \psi(l)}\Big|_{(U,V)} = 0 \qquad l = 1, 2, \ldots, M \tag{9}$$

The routine ways to solve these nonlinear equations are numerical and time-intensive (e.g. Yuan et al., 1992). However, if $\cos(\psi(l))$ and $\sin(\psi(l))$ are considered as two independent variables, rather than $\psi(l)$, we may have pairs of linear equations as follows:

$$\frac{\partial F}{\partial(\cos\psi(l))}\Big|_{(U,V)} = 0 \qquad \frac{\partial F}{\partial(\sin\psi(l))}\Big|_{(U,V)} = 0 \qquad l = 1, 2, \ldots, M \tag{10}$$

Once Eq. (10) is solved, some adjustment to the pairs is required in order to guarantee that they are always on the unit circle.

By solving Eqs. (8) and (10) iteratively, the optimal displacements at nodes and rotational angles of the elements are obtained, for a certain resolution. For plane problems, over-determination of the nonlinear equations is most likely to introduce an area increase or loss in each element during the retro-deformation. Area conservation in an individual element should be held to a minimal degree at the cost of continuity of retro-deformation between abutting elements.

2.3. Procedure

The procedure to apply this method to a geological problem is:

1. Discretize the deformed region into a series of 4-node tetrahedron elements in 3D cases or 3-node triangular elements in 2D cases. The number of elements depends on the variation of measured strain.
2. Choose the stationary node and the element with no rotation in the retro-deformation, based on the characteristics of deformational structures of interest.
3. Determine the strain in an individual element through interpolation of the measured strain data.
4. Let $i = 0$ and rotational angles $\psi^{(0)} = 0$.
5. Solve Eq. (8) for the displacements ($U^{(i)}$, $V^{(i)}$) with the given rotational angles $\psi^{(i)}$.
6. Solve Eq. (10) for rotational angles $\psi^{(i+1)}$ with the given displacements ($U^{(i)}$, $V^{(i)}$).
7. Compare the displacements at the ith iteration with those at the $i-1$th iteration. If their difference is unacceptable, let $i = i + 1$ and return to step 5. Otherwise stop the iteration and output the result.

Our calculation below has indicated that the algorithm is very effective in the first few iterations and that convergence becomes slower afterwards (Fig. 1).

3. Case study

3.1. Geology

The example we selected to test using the above technique is from the Fangshan granodioritic pluton (FGP), west of Beijing, central North China (Fig. 2). It is well studied from a geological, geochemical and geochronological perspective (Chen and Zhang, 1983; Liu and Wu, 1987; Ma, 1988; Hebei Bureau of Geology, 1989; Zhang, 1990; Zhang and Li, 1990). The pluton is slightly elliptical in map view with a mean diameter of 7 km, the long axis approximately trending toward the NW–SE direction. Mid-Proterozoic–Permian platformal carbonate and clastic sediments, as well as Lower Jurassic lacustrine and fluvial sediments, were intruded by the FGP. In general, a sharp contact exists between the FGP and its wall rocks. Strata were to some extent deflected in the vicinity of the FGP and thinned with respect to regional stratigraphic units. This attenuation reached a maximum near the western margin where the almost vertically dipping Paleozoic formations were in concordant contact with the FGP. Regionally, these strata were folded, thrusted and subjected to regional low-grade metamorphism (refined to the southern part of the region) during the late Jurassic to early Cretaceous, when Mesozoic tectono-magmatism culminated in North China Platform (Yih, 1920; Wang, 1951; Bao et al., 1983; Hebei Bureau of Geology, 1989; Shan et al., 1989, 1990; Davis et al., 2001).

Emplacement of the FGP occurred at approximately 2–3 km depth in the upper crust (Shan and Li, 1998). The FGP has a K–Ar whole rock age of ca. 132 Ma (Hebei Bureau of Geology, 1989). Isotopic ages on different minerals with varying blocking temperatures reveal its relatively long cooling history of several tens of millions of years (Chen and Zhang, 1983), suggesting the presence of an abnormally hot state in the wall rocks associated with contemporary low-grade regional metamorphism (Shan and Li, 1998). Furthermore, mass and heat transfer from the intrusive body caused an aureole of contact metamorphism in the wall rocks around the FGP, superimposed on regionally low-grade metamorphosed rocks (Liu and Wu, 1987).

Based upon petrology and contact relationships, three

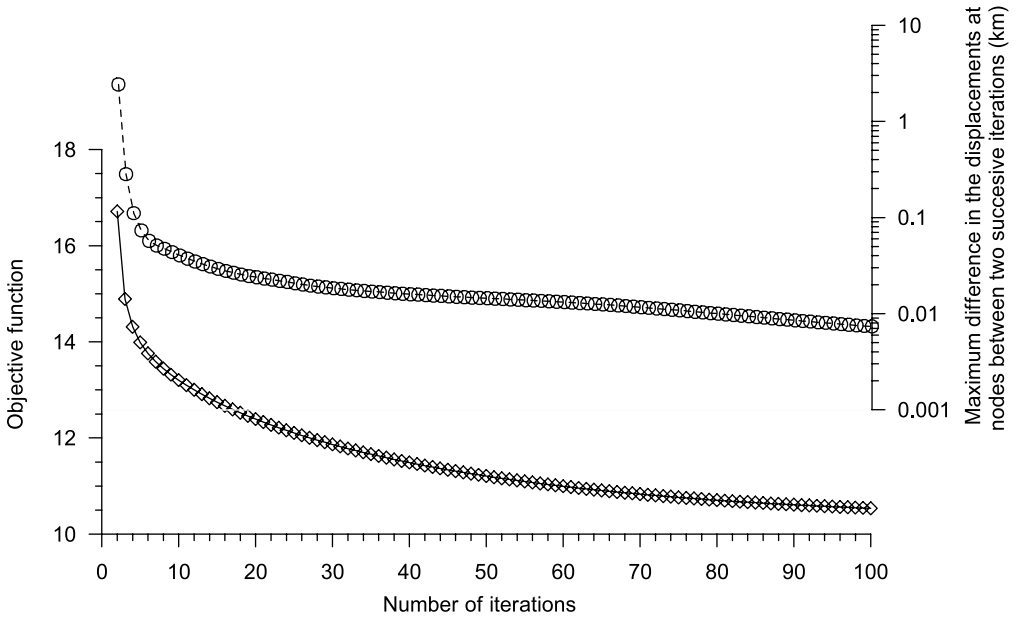

Fig. 1. The iteration number vs. the minimum of the objective function (solid line with diamonds) and the iteration number vs. the maximum difference in the displacement at nodes between two successive iterations (dashed line with blank circles).

main petrographic zones of the FGP are recognized: the marginal, transitional and central zones (Fig. 2b; Hebei Bureau of Geology, 1989). They consist of fine-grained quartz diorite, middle-grained quartz diorite and coarse-grained granodiorite, respectively. These have the shape of concentric rims representing successive magma pulses. Planar flow structures, which are alignments of planar and linear minerals in rocks and of elongated enclaves and xenoliths, are well developed in the marginal and transitional zones. They are approximately parallel to the outer rims of the zones, and commonly have a high dip angle of more than 70°, except for in the southeastern part where the dip ranges between 30° and 50° (Zhang, 1990; Zhang and Li, 1990). Linear flow structures are also frequently observed in these zones. In the western margin, instead of flow structures, there is the gneissic foliation and an overprint of small-scale ductile shear zones (Li, 1990). The FGP contains multiple generations of a large number of syn- and post-solidification fractures in concentric, radial and other patterns.

Forceful emplacement of the FGP is ascertained by numerous geological observations in outcrop, some of which have been described above. Based on these data—sharp contacts, stratigraphically-thinned wallrocks, concordant foliations in the wallrock and outer edge of the pluton—several geologists have interpreted emplacement of the FGP as resulting from a ballooning mechanism (e.g. Ma, 1988; Zhang, 1990; Zhang and Li, 1990). However, a majority of synchronous granite plutons in the North China Platform do not possess these characteristics diagnostic of forceful emplacement (Fig. 2a). These plutons were also emplaced between the middle Jurassic and the early Cretaceous, during a time of orogenesis in the eastern part of the North China Platform (Hebei Bureau of Geology, 1989; Davis et al., 2001).

3.2. Strain data

Enclaves of mostly dark diorite and to a lesser extent feldspar-rich amphibolite and hornblende-rich diopsidite and xenoliths of metamorphosed sandstone are frequently observed in the FGP. They are typically elongated and parallel to the flow or schist structures. Only the mafic enclaves were chosen to measure strain because of their abundance and easy recognition in outcrop. Strain data that we will use below are adopted from Zhang (1990) and shown in Fig. 3a. The axial ratio of strain is about one in the center where macroscopic plastic deformation is hardly observed in enclaves of equant shape. Strain intensity increases towards the margins and reaches a maximum in the western part of the FGP where the flow structures are replaced by intensive foliation. Strain intensity increases less in the southeastern marginal parts. The Flinn parameters calculated from the measured strain data are almost equal to zero, indicating the presence of an oblate strain state (Zhang and Li, 1990). Field observation of different kinds of strain markers reveals that the maximum or the intermediate principal strain in the outer zones tends to be parallel to the rims, and that the minimum principal strain is approximately horizontal.

Considering the approximately equant shape of enclaves in the less deformed rocks, it is clear that elongation of the enclaves in the FGP took place during the solidification and records the syn-emplacement deformation in rocks. Since

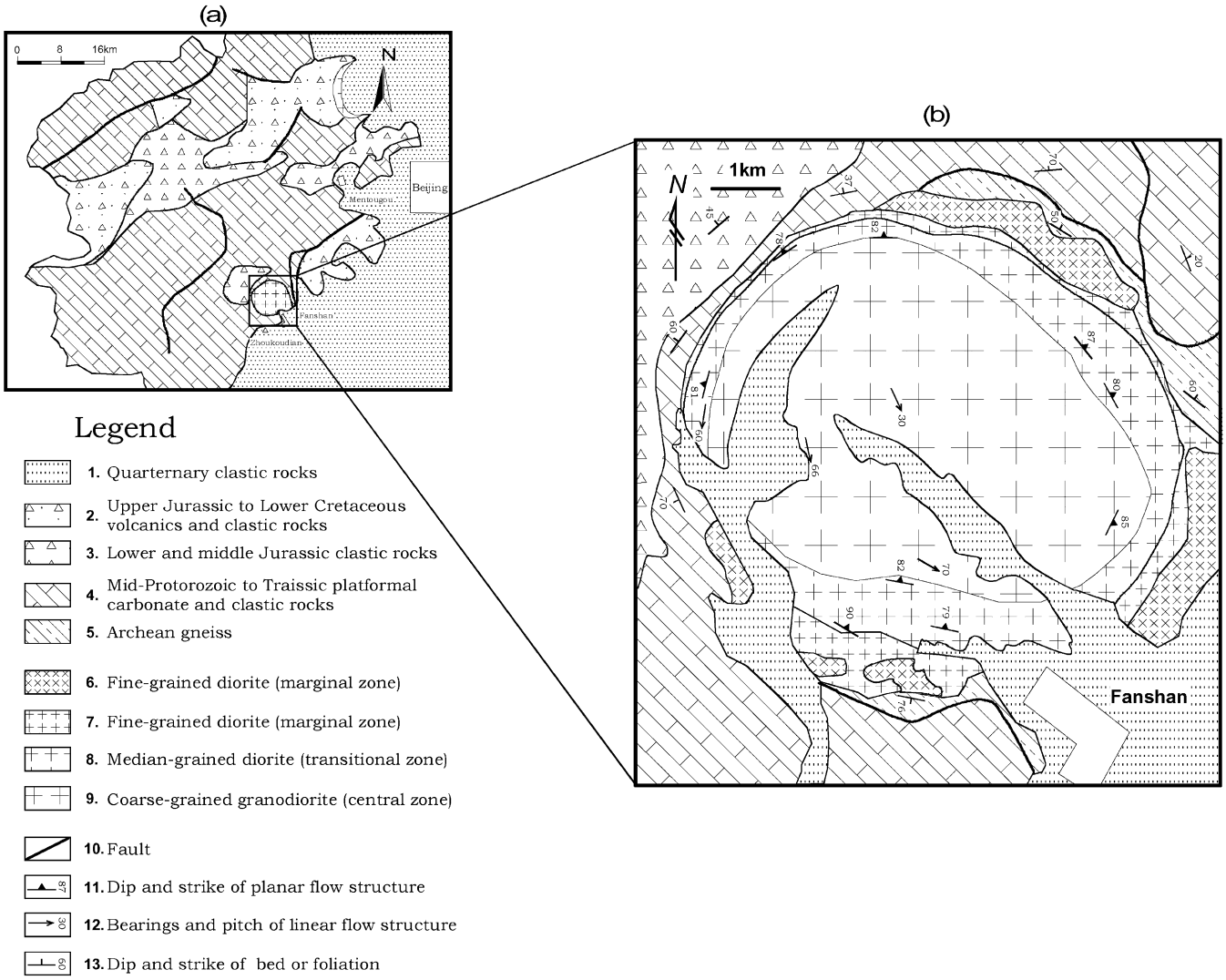

Fig. 2. Simplified geological maps of the study area, west of Beijing, northern China (modified from Hebei Bureau of Geology, 1989).

we have little knowledge about the difference in viscosity between the enclaves and the subsolidus matrix, the measured strain data may not perfectly record the average strain. But we have to assume that the strain recorded in enclaves is representative of the average strain in rocks, upon which our restoration of the outer zones is based.

3.3. Restoration

Since the marginal and transitional zones are only one quarter of the map view exposure of the FGP and since there are limited measured strain data in these zones, we combine the two outer zones (Fig. 2b) into a new zone (Fig. 3a). The new zone is discretized into a number of 93 3-node triangular element domains (Fig. 3b), the size of which is dependent upon the variation of measured strain. Nearly vertical flow structures and foliations as well as measured strain data indicate an oblate strain state or $t_1' \approx t_2' > t_3'$ where t_1', t_2' and t_3' are the half lengths of the maximum, the intermediate and the minimum principal strains, and that the minimum principal strain lies approximately in horizon. Hence we can reduce the 3D restoration of the new zone to a 2D restoration in the horizontal plane, although it is out of the plane deformation. In this plane case, the half lengths of the greatest and the least strains at any point, or t_1 and t_2, are directly calculated from the strain data at that point (Fig. 3a):

$$t_1 = \sqrt[3]{R^2}, \qquad t_2 = \frac{1}{\sqrt[3]{R}} \tag{11}$$

where R is the axial ratio of strain measured on the horizontal surface, equivalent to t_1/t_2.

The average strain in an individual element is obtained in the following two steps (Fig. 3c). First, the greatest principal direction in each element is determined by finding out the

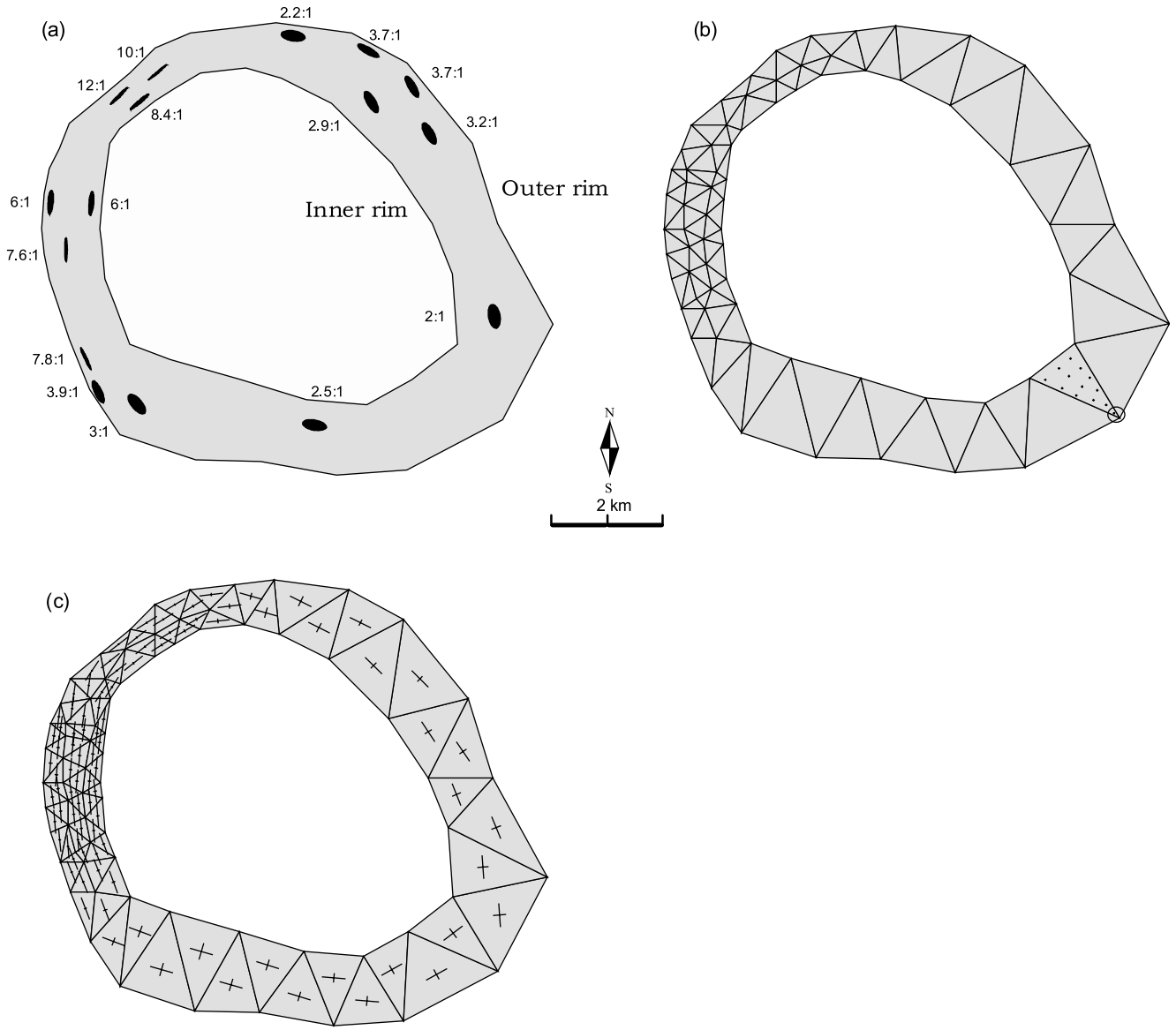

Fig. 3. (a) Strain data at some localities in the marginal and transitional zones (adopted from Zhang, 1990), assuming equi-dimensional shape of the enclaves in the undeformed state. At each locality, the strain datum represents the geometrical average of more than 30 strain data from flattened mafic enclaves measured in the approximately horizontal exposures. Measured strain generally varies a little from mafic enclaves, but greatly from enclaves having other rock type or xenoliths. (b) Discretization of the outer zones where the node circled is stationary and the elements with ' + ' marks have zero rotation during retro-deformation. The choice of the node and the element is based upon the symmetrical configuration of the FGP. (c) Strains in elements interpolated from those measured strain data in (a). The greatest principal strain has a constant length whereas the least principal strain varies in length according to the axial ratio of strain of the element.

tangential direction along the center of the element on the circle having the same center as the FGP has. They are approximately parallel to each other because of concentric emplacement of the FGP. Second, the axial ratio of strain in each element is interpolated from the measured data in Fig. 3a. The thin-plate spline method (Duchon, 1975) is adopted for construction of the interpolation function, by which strain ratio in each domain is interpolated from the measured strain data (Fig. 3a). This method is valid for a particularly small number of measured data.

Our object is to apply the technique to determine whether the volume space, or the area within the inner rim of the new zone containing the central zone can be explained by retro-deforming or not. Results of the application of our technique are shown in Table 1 and Figs. 1, 4 and 5. In Fig. 1, the algorithm is very effective in the first iterations but becomes slower to converge afterwards. It usually takes a large number of iterations to reach a given resolution. A 10-m-resolution is set up in the restoration, for which no more than 100 iterations are enough to guarantee convergence.

Table 1
Shrinkage of the restored zone after different number of iterations

Iterations	F	D_{max} (km)	The area within the outer rim			The area within the inner rim		
			Deformed (km^2)	Restored (km^2)	Error proportion	Deformed (km^2)	Restored (km^2)	Error proportion
1	612.00		96.01	86.60	10%	49.07	10.94	78%
25	12.10	0.0206		74.48	22%		7.81	84%
50	11.21	0.0144		72.42	25%		8.63	82%
75	10.76	0.0108		71.01	26%		9.78	80%
100	10.54	0.0074		70.11	27%		10.81	78%

Notes: F is the minimum of the objective function and D_{max} is the maximum difference in the displacements at nodes between two successive iterations. The error proportion is defined as: $(W_i - W_f)/W_f \times 100\%$ where W_i and W_f are observed values of one variable in the deformed and the restored states, respectively.

Although more iterations will increase the precision of the displacement solution at nodes, it is not worth the cost of extended running time. The restored shape does not appear to vary distinctly with the number of iterations (no less than 25; Fig. 4).

The restored zone is approximately elliptical in shape, the long axis exceeding the mean diameter of the FGP (Fig. 5a). This is an unrealistic shape, which we will discuss below. The area within the outer rim of the restored zone has an area of 70.1 km^2 (~27% of the original area of the FGP), whereas the area within the inner rim has an area 10.8 km^2 (~78% of the original area of the present inner zone). It is obvious that retro-deformation has produced an intense shrinkage towards the center of the FGP (Fig. 5a), especially on the inner rim. However, there still remains an area within the restored inner rim that cannot be restored in this way and needs another explanation. Since the restoration is concerned only with flow/plastic deformation recorded by the elongated enclaves in the FGP, the fracturing process must have absorbed some part of the radial inflation associated with the emplacement of the central zone. It is difficult to recognize in outcrop syn- and post-solidification fractures in the outer zones formed during the emplacement of the inner zone, but they appear to be comparatively small. Furthermore, we have not taken into account the misfit between the restored and the real shapes caused by a variety of factors that we discuss below.

Restorable strain is referred to as some part of interpolated strain in an individual element that can be recovered in retro-deformation. It is generally close to the strain interpolated in each element (compare Fig. 5b with Fig. 3c). The rotational angle is rather small in most elements except for those where the interpolated strain varies distinctly. Large rotation angles, for instance, occur in the northwestern part and in the southern part (Fig. 5c).

3.4. Implications

From the reduced 2D restoration, a scenario of the emplacement of the central zone of the FGP is envisioned. Before its emplacement, the intruded magma at depth was probably circular or slightly elliptical in plan view as the FGP is now, comprising ca. 75% of the present FGP. Apart from the western margin, solid-state plastic deformation in response to the later inflation is seldom observed in magmatic rocks of the outer zones (Ma, 1988; Zhang and Li, 1990). Therefore, solidification of the intruded magma must have continued until the emplacement of the central zone. During the emplacement, the intruding magma inflated the surrounding rocks in a radial pattern with additional intensification of strain toward the western margin. Both subsolidus rocks in the outer zones and the wall rocks around the FGP underwent intense contraction to provide room for its emplacement. In the outer zones, most of the inflation was absorbed in the form of flow/plastic deformation, because a majority of the area within the inner rim can be restored.

Depending on the involvement of the wall rocks, two end-member models of flow/plastic deformation in the outer zones are discriminated. The deformation in the first model is confined to the outer zones whereas in the second model deformation occurred in both the wall rocks and the outer zone. These two end members are characterized by a difference in rock stiffness between the wall rocks and rocks in the outer zones. The first model requires less forceful emplacement than the latter. Their roles in creating room can be roughly determined from the result of the above-mentioned restoration (Fig. 5; Table 1). The result of the second model is characterized by a difference in the area within the outer rim between the present state and the restored state. The area within the outer zone presently occupies 25.9 km^2, nearly half of the area within the inner rim. Therefore, either model may be applicable, but both require forceful emplacement of the FGP.

In addition, vertical expansion had played an important role in creating space for the subsequent emplacement, because of the oblate strain state in the outer zones. This

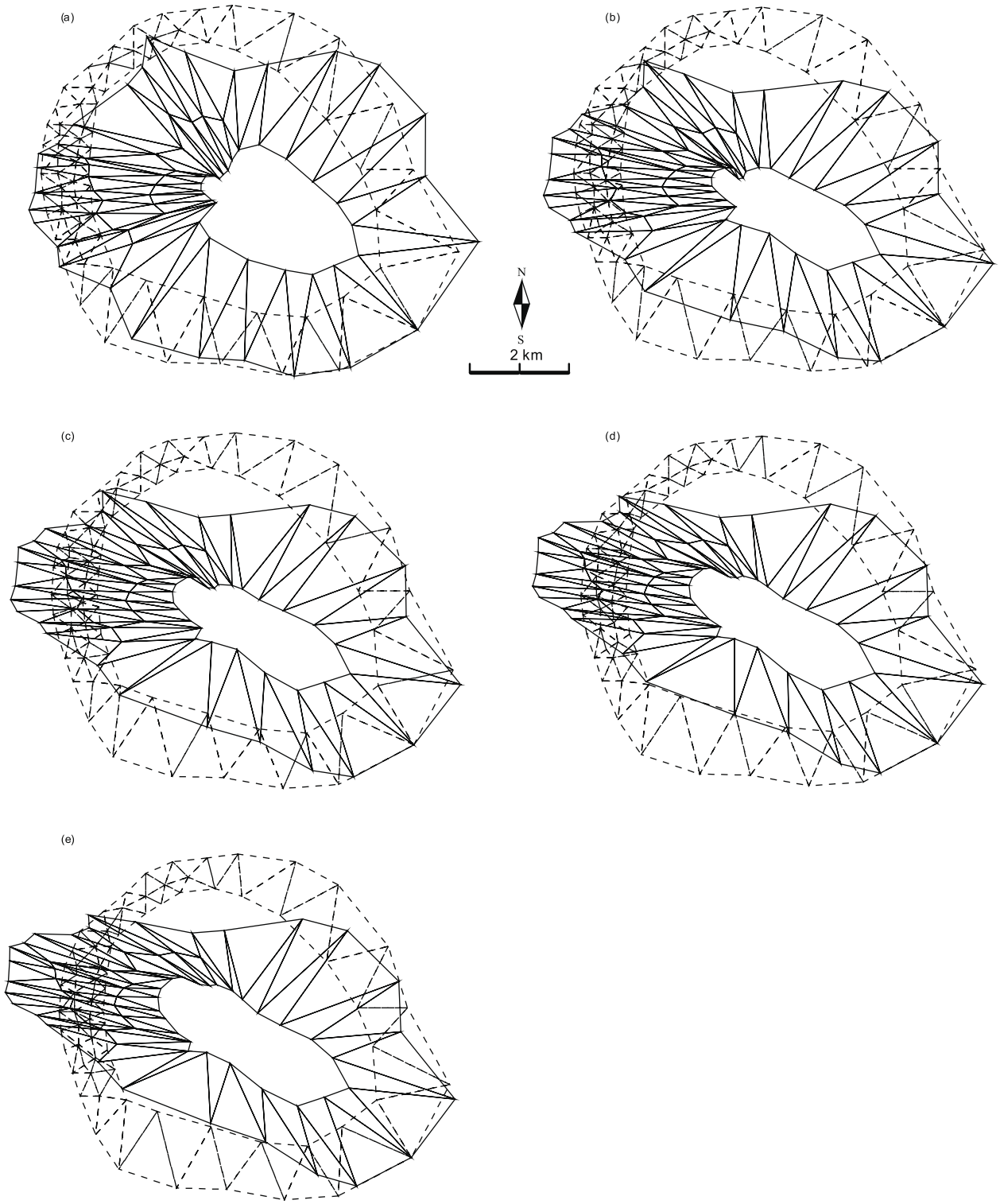

Fig. 4. The present deformed shape (dashed lines) vs. the restored (dark lines) of the new zone of the FGP after different iterations: 0 (a), 25 (b), 50 (c), 75 (d) and 100 (e).

affect can be evaluated by the above restoration. The area within the outer zones is 46.94 km^2 in the present state and 59.3 km^2 in the restored state. Since there is no area loss/gain in the retro-deformation, the difference of 12.26 km^2 must be accounted for by vertical expansion. The value is relatively low compared with the restorable area within the inner rim in the present state, 38.16 km^2. It seems that vertical expansion is less effective in creating

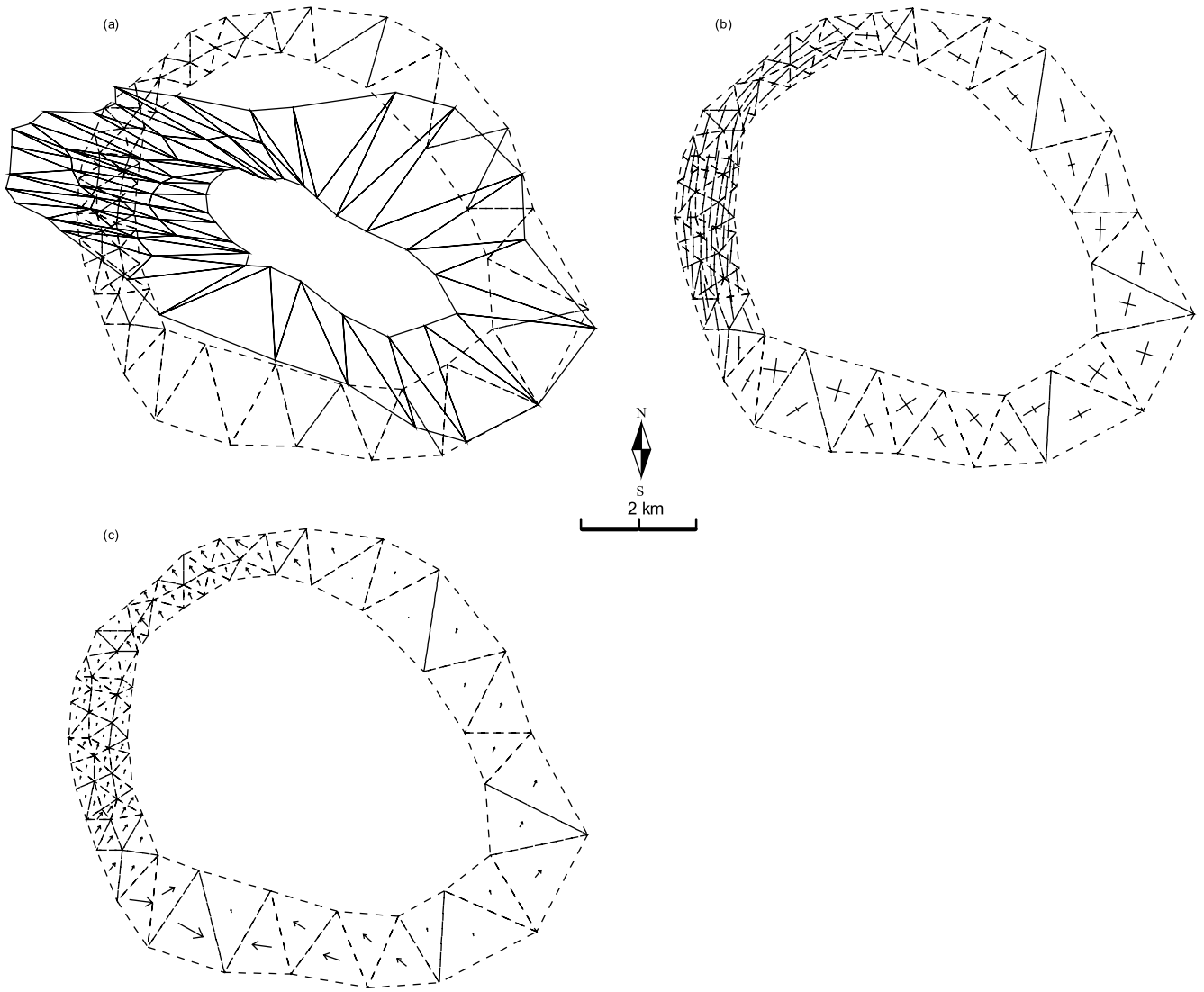

Fig. 5. Restoration of the new zone after 100 iterations, the restored shape (black lines) vs. the present deformed shape (dashed lines) (a), restorable strain in elements (b), and rotational angles in elements (c). The direction of vertical arrows relative to north represents rotational angles, and the length of the arrow is proportional to the rotational angle. See Fig. 3 for further explanation.

space than lateral expansion, the former only producing near one third of the area created by the latter.

4. Discussion and conclusion

4.1. Methodology

A new technique is presented in this paper to restore deformed shapes in a continuous way by the minimization of the difference between measured and theoretical reverse displacement gradients. It is in the category of continuous restoration and different from existing restoration techniques (Oertel and Ernst, 1978; Cobbold, 1979; Cobbold and Percevault, 1983; Woodward et al., 1986; Howard, 1993; Rouby et al., 2000; Lamb, 2001). In spite of complications due to the use of the finite element concept, our technique is direct and objective. Through construction of reverse displacement gradients, the continuity of the displacement across the boundary between abutting element domains is ensured. Additional distortion of the elements, resulting from the incompatibility of interpolated strain between abutting elements, is kept at a minimum. The process automatically seeks the optimum reverse displacement gradient at a given resolution. What is more important, the technique can be slightly modified to cope with discontinuous deformation, faults for instance, like the method of Rouby et al. (2000). As shown in another paper (Shan et al., 2002), an extension of the technique is applicable to discontinuous deformation. Fault shapes can be addressed, for instance, by imposing constraints on the restored cutoff lines along the faults—the nodes on the

cutoff line in the hanging wall must be fit into the cutoff line in the footwall after restoration; and vise versa. That is to say, if possible in the restored state, the nodes on the cutoff line in one sidewall are in the cutoff line in the other sidewall. These constraints are linear and can be directly added to the above-mentioned over-determined equations (Shan et al., 2002).

At the cost of compatibility of retro-deformation between abutting elements, the restorable strain in elements does not commonly correspond with the interpolated strain. The interpolated strain may be incompatible across the boundary between abutting elements. This will cause misfit of the restored shape with the real one. The misfit is dependent upon many possible factors, including size and shape of element domains, the assumption of homogeneous deformation in elements, reduction in dimension of deformed shapes, the interpolation function of measured strain data, errors in the measurement of strain, and so forth. The latter three factors are common and their discussion is beyond of the scope of this paper. In nature, homogeneous deformation in the triangular domains is generally inconsistent with the real deformation. The common way to alleviate deformational heterogeneity is adjustment of the mesh size according to the variation of measured strain. The larger the variation of measured strain, the smaller the mesh size. In the above example, we believe that the discretization is the main factor responsible for the unrealistic restored shape of the new zone (Figs. 4 and 5). Optimization of the mesh through minimization of incompatibility of interpolated strain between abutting elements is a subject for further study.

4.2. Emplacement mechanism

How pluton emplacement is accommodated by the interaction among regional deformation, deformation of wall rocks and the accenting/stopping magma is an intriguing issue. In general, any deformation can be described by a combination of pure strain, rotation and translation, and this is a particularly useful way to look at pluton emplacement (Tikoff et al., 1999). Among the three deformation components, translation and rotation are not recorded by strain markers and quantification of these requires palinspastic restoration. The method presented in this paper provides a way of quantifying these parameters. Since it utilizes a minimization technique, estimates for these parameters are conservative.

Our technique was applied to the Fangshan granodioritic pluton (FGP), in central North China. By using the current outcrop shape of the pluton and the strain recorded in the wallrock, the method solves for displacements. One difficulty of our approach is that the strain estimates for the enclaves were not calibrated in terms of a viscosity contrast between the deformed enclaves and the matrix. Thus, our restoration is only strictly applicable if the enclaves are good markers of finite strain.

Our modeling indicated that about 78% area of the present central zone could be restored by retro-deformation of the marginal and transitional zones. Much of the space for emplacement of the inner zone was apparently created through plastically expanding the outer zones and wallrock. Deformation, as a result of the emplacement of the central zone, occurs by flow/plastic deformation in the marginal zone, transitional zone, and wallrocks. A large part of this retro-deformation also involved translation of the outer zone and wallrocks. Rotation was generally not large, but reached a maximum on the north and south sides of the pluton. These conclusions are similar to those of Guglielmo (1994), although his forward modeling is distinctly different from the approach outlined in this manuscript. In addition, two end-member deformation models are considered, which either include or exclude strain in the wallrocks. Both models have similar results. In addition to lateral expansion, vertical expansion also produced near one third of the volume created by later intrusion.

Based upon the restoration, we argue that a ballooning mechanism best describes the forceful emplacement of the FGP. Similar to other studies of ballooning plutons—such as the Cannibal Greek pluton in Australia (Davis, 1993), the Papoose Flat pluton in California (de Saint Blanquet et al., 2001) and the Mono Greek granite in the Sierra Nevada (Tikoff et al., 1999)—both internal strain and translation of the surrounding material were inferred to occur during pluton emplacement to make space for the intruding pluton. The thinning of the stratigraphy around the FGP is similar to that of the Papoose Flat pluton in California (de Saint Blanquet et al., 2001). The forceful emplacement of the FGP must have involved forces large enough to push the wallrocks aside. These conditions are probably satisfied in the region, as the FGP was emplaced during low-grade regional metamorphism.

Acknowledgements

This research was supported by the Chinese Academy of Sciences, the CAS program (Program No: KZCX2-113) and the Shandong Natural Science Foundation, Grant Y98E08078. Most of the work was done in the “Laboratory for Numerical Simulation of Continental Deformation and Dynamics” in the Changsha Institute of Geotectonics, the Chinese Academy of Sciences. Dr B. Tikoff at Wisconsin University, USA, and Dr C.B. Zhao in CSIRO are thanked for the substantial English improvement of this article. B. Tikoff, P.R. Cobbold, E. de Kemp and three anonymous referees of JSG are appreciated for their critical reviews and suggestions.

Appendix A

List of symbols and their definitions

Symbols	Definitions	Comment
(x_0, y_0, z_0)	The Cartesian coordinate of a material point P_0 in the deformed state	See Eq. (1)
(x_1, y_1, z_1)	The Cartesian coordinate of a material point P_1 in the undeformed state	The point P_0 becomes P_1 after retro-deformation; see Eq. (1)
(x_i, y_i)	The Cartesian coordinates at nodes of a 2D element	$i = 1, 2, 3$; see Appendix B
(U, V, W)	(1) The displacement at the point P_0, and (2) the displacements at all nodes	See Eqs. (1)–(4) and (6)–(10)
$(\Delta U, \Delta V)$	An incremental translation of the elements	
$(U^{(i)}, V^{(i)})$	The displacements at nodes after a number of i iterations	
(U_i, V_i, W_i)	The displacement at the ith local node of an individual element	See Eqs. (3) and (4)
$(U(l), V(l), W(l))$	The displacement at the nodes of the lth element	See Eqs. (7) and (8)
ψ or $\psi(l)$	Rotational angle of an individual element or of the lth element in 2D	See Eqs (6), (7), (9) and Appendix C
$\psi^{(i)}$	The rotational angles at the ith iteration in 2D	
$\Delta\psi$	Any rotation of the elements	
k	The number of nodes of an individual element	It is three for the 3-node triangular element
M	The number of total elements in the deformed region	
L	The number of total nodes in the deformed region	
T	Theoretical reverse displacement gradient	A 3×3 or 2×2 tensor, see Eq. (4)
t_{ij} or t_{ijl}	An element of the matrix T for an individual element or for the lth element	See Eqs. (4) and (7)
C	Observed reverse displacement gradient	A 3×3 or 2×2 tensor, see Eq. (5)
c_{ij} or c_{ijl}	An element of the matrix C for an individual element or for the lth element	See Eqs. (5) and (7)
A	The transformation unstraining a deformed block	See Appendix C
a_{ij}	An element of the matrix A	See Appendix C
t_1', t_2' and t_3'	The half lengths of the maximum, the intermediate and the minimum principal strains	
t_1 and t_2	The half lengths of the greatest and the least strains in 2D	See Eqs. (5) and (11) and Appendix C
θ	The direction of the greatest strain in 2D	See Eq. (5) and Appendix C
R	Axial ratio of strain in a 2D block	See Eq. (11) and Appendix C
N_i	The shape function	See Eq. (4) and Appendix B
a_i, b_i and c_i	The constants of the N_i for a triangular element	See Appendix B
S	The area of a triangular element	See Appendix B
F	The objective function	See Eq. (7) and Table 1
$D_{\max}$	The maximum difference in calculated displacements at nodes between two successive iterations	See Table 1
(Xt, Yt)	Translation of a block in 2D	See Appendix C

Appendix B. Definition of the local function

As stated in the text, we assume homogeneity of deformation in each element. This corresponds with the construction of a linear local function for interpolation of the displacement at any point of the element from the displacements at nodes. It is rather easy to write out the formula of linear local functions in 2D and 3D cases, but only in the 2D case will be listed below. Let ΔABC be a 3-node triangular element (Fig. A1). The linear local function of any point (x, y) in the element is defined as (Zienkiewicz, 1977):

$$N_i(x, y) = \frac{1}{2S}(a_i + b_i x + c_i y), \quad i = 1, 2, 3 \tag{A1}$$

where S is the area of the study triangular, and coefficients a_i, b_i and c_i are constants. They are the functions of the coordinates at the nodes:

$$S = \tfrac{1}{2}(x_1y_2 - x_2y_1 + x_3y_1 - x_1y_3 + x_2y_3 - x_3y_2) \tag{A2}$$

$$a_1 = x_2y_3 - x_3y_2$$

$$b_1 = y_2 - y_3$$

$$c_1 = x_3 - x_2$$

$$a_2 = x_3y_1 - x_1y_3$$

$$b_2 = y_3 - y_1$$

$$c_2 = x_1 - x_3$$

$$a_3 = x_1y_2 - x_2y_1$$

$$b_3 = y_1 - y_2$$

$$c_3 = x_2 - x_1$$

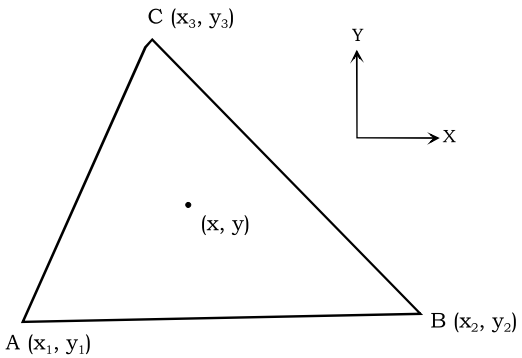

Fig. A1. A diagram of a 3-node triangular element.

Appendix C. Measured reverse displacement gradient

Suppose the deformation in a 2D block is homogeneous. Its reverse displacement field is composed of translation, rotation and deformation. Let (Xt, Yt) stand for the translation, θ for the orientation of the maximum principal strain, t_1 and t_2 for the half lengths of the maximum and the minimum principal strains, and Ψ rotational angle (Fig. A2). Both t_1 and t_2 are calculated from the known axial ratio of strain (R) and the known strain state in the block. For example in pure-shear plane deformation, they are:

$$t_1 = \sqrt{R}, \qquad t_2 = \frac{1}{\sqrt{R}} \tag{A3}$$

Restoration of the deformed block is sequentially made by exerting on it the translation of ($-Xt$, $-Yt$), rotation with an angle of $-\Psi$ and deformation with (t_1, t_2, $\pi/2+\theta$). This operation is easily done in terms of a matrix with each manipulation representing a different transformation. For the sake of convenience, we assume

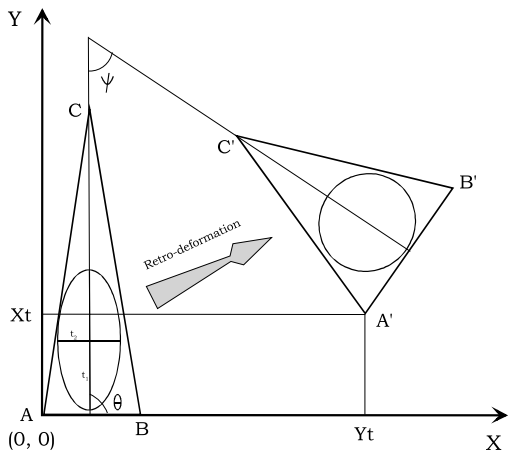

Fig. A2. Retro-deformation of the ΔABC element in the deformed state to the ΔA′B′C′ element in the restored state.

that block rotation took place before its deformation, although the final transformation is often different from that with rotation after deformation. The reverse displacement (U, V) of any point (x, y) in the block is:

$$\begin{aligned}
\begin{bmatrix} U \\ V \end{bmatrix} &= -\begin{bmatrix} x \\ y \end{bmatrix} - \begin{bmatrix} Xt \\ Yt \end{bmatrix} + \begin{bmatrix} \cos(-\psi) & -\sin(-\psi) \\ \sin(-\psi) & \cos(-\psi) \end{bmatrix} \\
&\times \begin{bmatrix} \cos\left(\frac{\pi}{2}+\theta\right) & \sin\left(\frac{\pi}{2}+\theta\right) \\ -\sin\left(\frac{\pi}{2}+\theta\right) & \cos\left(\frac{\pi}{2}+\theta\right) \end{bmatrix} \\
&\times \begin{bmatrix} t_1 & 0 \\ 0 & t_2 \end{bmatrix} \\
&\times \begin{bmatrix} \cos\left(\frac{\pi}{2}+\theta\right) & -\sin\left(\frac{\pi}{2}+\theta\right) \\ \sin\left(\frac{\pi}{2}+\theta\right) & \cos\left(\frac{\pi}{2}+\theta\right) \end{bmatrix} \begin{bmatrix} x \\ y \end{bmatrix} \\
&= -\begin{bmatrix} x \\ y \end{bmatrix} - \begin{bmatrix} Xt \\ Yt \end{bmatrix} + \begin{bmatrix} \cos(-\psi) & -\sin(-\psi) \\ \sin(-\psi) & \cos(-\psi) \end{bmatrix} \\
&\times \begin{bmatrix} \cos^2(\theta)t_1 + \sin^2(\theta)t_2 & \sin(\theta)\cos(\theta)(t_1 - t_2) \\ \sin(\theta)\cos(\theta)(t_1 - t_2) & \sin^2(\theta)t_1 + \cos^2(\theta)t_2 \end{bmatrix} \\
&\times \begin{bmatrix} x \\ y \end{bmatrix}
\end{aligned} \tag{A4}$$

Let matrix A be:

$$A = \begin{bmatrix} a_{11} & a_{12} \\ a_{21} & a_{22} \end{bmatrix}$$

$$= \begin{bmatrix} \cos^2(\theta)t_1 + \sin^2(\theta)t_2 & \sin(\theta)\cos(\theta)(t_1 - t_2) \\ \sin(\theta)\cos(\theta)(t_1 - t_2) & \sin^2(\theta)t_1 + \cos^2(\theta)t_2 \end{bmatrix} \tag{A5}$$

The matrix A is to unstrain the deformed block

without taking rotation into account and is calculated from the known strain in the block. Hence we have:

$$\begin{bmatrix} U \\ V \end{bmatrix} = -\begin{bmatrix} x \\ y \end{bmatrix} - \begin{bmatrix} Xt \\ Yt \end{bmatrix} + \begin{bmatrix} \cos(-\psi) & -\sin(-\psi) \\ \sin(-\psi) & \cos(-\psi) \end{bmatrix} \begin{bmatrix} a_{11} & a_{12} \\ a_{21} & a_{22} \end{bmatrix} \begin{bmatrix} x \\ y \end{bmatrix}$$
$$= \begin{bmatrix} (a_{11}\cos(-\psi) - a_{12}\sin(-\psi))x + (a_{21}\cos(-\psi) - a_{22}\sin(-\psi))y - x - Xt \\ (a_{11}\sin(-\psi) + a_{12}\cos(-\psi))x + (a_{21}\sin(-\psi) + a_{22}\cos(-\psi))y - y - Yt \end{bmatrix} \quad \text{(A6)}$$

By differentiating the above equations, we obtain the reverse displacement gradient in the following:

$$\begin{bmatrix} \frac{\partial U}{\partial x} & \frac{\partial U}{\partial y} \\ \frac{\partial V}{\partial x} & \frac{\partial V}{\partial y} \end{bmatrix} = \begin{bmatrix} a_{11}\cos(-\psi) - a_{12}\sin(-\psi) - 1 & a_{21}\cos(-\psi) - a_{22}\sin(-\psi) \\ a_{11}\sin(-\psi) + a_{12}\cos(-\psi) & a_{21}\sin(-\psi) + a_{22}\cos(-\psi) - 1 \end{bmatrix} \quad \text{(A7)}$$

References

Bao, Y.G., Xie, D.Y., Chen, Z.B., Mu, B.T., 1983. On the Yanshanian movement in the region of Beijing (in Chinese with an English abstract). Acta Geologica Sinica 57, 195–204.

Chen, B., 1996. Optimum Theory and its Algorithms, Qinghua University Press, Beijing, (in Chinese).

Chen, X.G., Zhang, G.K., 1983. Determination of fission track ages in the Fangshan granodioritic pluton, Beijing. Chinese Science Bulletin 28, 339–357. (in Chinese).

Cobbold, P.R., 1979. Removal of finite deformation using strain trajectories. Journal of Structural Geology 1, 67–72.

Cobbold, F.R., Percevault, M.-N., 1983. Spatial integration of strains using finite elements. Journal of Structural Geology 5, 299–305.

Davis, B.R., 1993. Mechanism of emplacement of the Cannibal Creek Granite with special reference to timing and deformation history of the aureole. Tectonophysics 234, 337–362.

Davis, G.A., Zheng, Y.D., Wang, C., Darby, B.J., Zhang, C.H., Gehrels, G., 2001. Mesozoic tectonic evolution of the Yanshan fold and thrust belt, with emphasis on Hebei and Liaoning provinces, northern China. Geological Society of America Memoir 194, 171–197.

Duchon, J., 1975. Splines minimizing rotation—invariant seminorms in Sobolev spaces. In: Schempp, W., Zeller, K. (Eds.), Multivariate Approximation Theory, Chapman and Hill, London, pp. 101–109.

Guglielmo, G., 1994. Interference between pluton expansion and coaxial tectonic deformation: Three-dimensional computer model and field implications. Journal of Structural Geology 16, 237–252.

Hebei Bureau of Geology, 1989. Regional Geology of Hebei Province, Geological Publishing House, Beijing, (in Chinese with an English abstract).

Hossack, J.R., 1978. The correction of stratigraphic sections for tectonic finite strain in the Bygdin area, Norway. Journal of the Geological Society of London. 135, 229–241.

Howard, J.H., 1993. Restoration of cross-section through unfaulted, variably strained strain. Journal of Structural Geology 15, 1331–1342.

Ismail-Zadeh, A.T., Talbot, C.J., Volozh, Y.A., 2001. Dynamic restoration of profiles across diapiric salt structures: numerical approach and its application. Tectonophysics 337, 23–38.

Lamb, S., 2001. Vertical axis rotation in the Bolivian orocline, South America 2. Kinematic and dynamic implications. Journal of Geophysical Research 106 (B11), 26,633–26,653.

Li, Z.Z., 1990. The microstructure of shear zone of Fangshan intrusion (in Chinese with an English abstract). In: Zhang, J.S., Shan, W.L. (Eds.), The Geological Study of Xishan, Beijing, The Press of China University of Geosciences, Wuhan, pp. 62–72.

Liu, G.H., Wu, J.S., 1987. Metamorphic belts in the area of Fangshan, Beijing (in Chinese with an English abstract). Bulletin of the Chinese Academy of Geological Sciences 16, 113–1137.

Ma, C.Q., 1988. The magma-dynamic mechanism of emplacement and compositional zonation of the Zhoukoudian stock, Beijing (in Chinese with an English abstract). Acta Geologica Sinica 62, 329–343.

Oertel, G., Ernst, W.G., 1978. Strain and rotation in a multilayered fold. Tectonophysics 48, 77–106.

Rouby, D., Xiao, H., Supper, J., 2000. 3-D restoration of complex folded and faulted surfaces using multiple unfolding mechanisms. The American Association of Petroleum Geologists Bulletin 84, 805–829.

de Saint Blanquet, M., Richard, D.L., Bouchez, J.-L., Morgan, S.S., 2001. Internal structure and emplacement of the Papoose Flate pluton: an integrated structural, petrographic, and magnetic susceptibility study. Geological Society of America Bulletin 113, 976–995.

Schultz-Ela, D.D., 1988. Application of a three-dimensional finite element method to strain analysis. Journal of Structural Geology 10, 263–272.

Schultz-Ela, D.D., Hudleston, P.J., 1991. Strain in an Archean greenstone belt of Minnesota. Tectonophysics 190, 233–268.

Schwerdtner, W.M., 1977. Geometric interpretation of regional strain analysis. Tectonophysics 39, 515–531.

Shan, W.L., Wang, F.A., Zhang, J.S., Song, H.L., Fu, Z.L., 1989. Tectonic evolution of the platformal layers in the Western Hills, Beijing (in Chinese with an English abstract). Earth Sciences 1, 37–44.

Shan, W.L., Zhang, J.S., Song, H.L., Fu, Z.L., 1990. The tectonic evolution in the southern part of the Western-Hill, Beijing (in Chinese with an English abstract). In: Zhang, J.S., Shan, W.L. (Eds.), The Geological Study of Xishan, Beijing, The Press of China University of Geosciences, Wuhan, pp. 1–7.

Shan, Y.H., Li, Z.A., 1998. The impact of regional metamorphism on the cooling history of the Fangshan Pluton, Beijing: a numerical approach (in Chinese with an English abstract). Modern Geology 12, 68–74.

Shan, Y.H., Suen, H.B., Li, Z.A., Lin, G., 2002. Restoration of three-dimensional deformed surfaces (in Chinese with an English abstract). Petroleum Exploration and Development 29 (5), 37–40.

Tikoff, B., de Saint Blanquat, M., Teyssier, C., 1999. Translation and the resolution of the pluton space problem. Journal of Structural Geology 21, 1109–1117.

Wang, C., 1951. On the chloritoid belt in the Western Hills of Peiking. Geological Society of China Bulletin 31, 1–4.

Woodward, N.B., Gray, D.R., Spears, D.B., 1986. Including strain data in balanced cross-sections. Journal of Structural Geology 8, 313–324.

Yih, Z.F., 1920. The Geology of Hsi-Shan or the Western Hills of Peking, Peking, The Geological Survey of China, Ministry of Agriculture and Commerce.

Yuan, W., Zhang, L., Huang, X., Wen, Z., 1992. Numerical Analysis, Southeastern University Press, Nanjing, (in Chinese).

Zienkiewicz, O.C., 1977. The Finite Element Method, McGraw-Hill, London.

Zhang, J.S., Li, Z.Z., 1990. Emplacement deformations and ballooning mechanism about Fangshan granodiorite pluton (in Chinese with an English abstract). In: Zhang, J.S., Shan, W.L. (Eds.), The Geological Study of Xishan, Beijing, The Press of China University of Geosciences, Wuhan, pp. 48–61.

Zhang, Z.J., 1990. The study of the tectonic stress field of Fangshan rock-body intrusion contact zone in West Hill, Beijing (in Chinese with an English abstract). In: Zhang, J.S., Shan, W.L. (Eds.), The Geological Study of Xishan, Beijing, The Press of China University of Geosciences, Wuhan, pp. 73–82.